# *Global warming drives a threefold increase in persistence and 1°C rise in intensity of marine heatwaves*

Article

Accepted Version

# Global warming drives a threefold increase in persistence and $1^{\circ}C$ rise in intensity of marine heatwaves

**Marta Marcos**[a,b,c], **Angel Amores**[a,b], **Miguel Agulles**[a], **Jon Robson**[d], **and Xiangbo Feng**[d]

This manuscript was compiled on January 31, 2025

**Marine heatwaves are extreme climatic events consisting of persistent periods of warm ocean waters that have profound impacts on marine life. These episodes are becoming more intense, longer and more frequent in response to anthropogenic global warming. Here we provide a comprehensive and quantitative assessment on the role of global warming on marine heatwaves. To do so, we construct a counterfactual version of observed global sea surface temperatures since 1940, corresponding to a stationary climate without the effect of long-term increasing global temperatures, and use it to calculate the contribution of global air temperature rise on the intensity and persistence of marine heatwaves. We determine that global warming is responsible for nearly half of these extreme events and that, on a global average, it has led to a three-fold increase in the number of days per year that the oceans experience extreme surface heat conditions. We also show that global warming is responsible for an increase of 1°C in the maximum intensity of the events. Our findings highlight the detrimental role that human-induced global warming plays on marine heatwaves. This study supports the need for mitigation and adaptation strategies to address these threats to marine ecosystems.**

Marine heatwaves | Climate change | Extreme event attribution |

## Significance Statement

Marine heatwaves are periods of persistent warm ocean waters that are becoming more frequent and intense due to global warming, posing increasing threats to vulnerable marine ecosystems. Here, we calculate the relationship between increasing global surface air temperature and local sea surface temperatures to quantify the role of anthropogenic forcing in the intensity and persistence of these climatic extreme events. We construct a counterfactual climate of sea surface temperatures in which the long-term trends linked to global warming have been removed but that contains internal variability and preserves the observed chronology. The comparison between observed and counterfactual sea surface temperatures reveals the dominant contribution of anthropogenic forcing to observed marine heatwaves, especially since year 2000.

Marine heatwaves (MHW), defined as persisting periods of prolonged warm ocean waters (1), pose severe threats to marine ecosystems (2), such as coral reefs (3), seagrass meadows (4) and kelp forests (5), and have detrimental impacts on the ecosystem services they provide (6). Over the last decades, MHW have been documented worldwide (7), with increasing frequency, duration and intensity (8, 9). Recent episodes of major MHW, like the exceptionally long Pacific MHW in 2014-15 (10), the intense event in the Tasman Sea in 2015-16 (11) and the record high sea surface temperatures around the UK and in the Mediterranean Sea during summer 2023*, have stimulated scientific research on these extreme climate events and contributed to raising public awareness of their impacts.

Over long multi-decadal time scales the enhanced intensity and frequency of MHW have been linked to anthropogenic ocean warming (7, 12, 13). Changes in Sea Surface Temperature (SST), a variable generally used to characterise MHW, confirm that the likelihood and intensity of MHW have evolved out of the bounds of natural variability (2, 8, 14, 15), pointing to the driving force of anthropogenic warming (9, 13), to the extent that around 87% of MHW observed between 2006 and 2015 are likely attributed to human-induced warming (7). Earlier studies have explored the contribution of human-driven global warming to MHW. For example, (11, 16) applied attribution frameworks to assess the changes in the probabilities of individual events under current climate conditions. Likewise, (2) compared the SST fields from climate models and pre-industrial control runs, evidencing changes in probability of occurrence and intensity of MHW. Also, (9) evaluated to which extent human-driven global warming has modified the likelihood of the observed global MHW during the satellite period since 1981. By comparing pre-industrial and present-day simulations of climate models, they concluded that the probabilities of the largest observed MHW events have increased at least 20-fold due to anthropogenic forcing.

A comprehensive and quantitative assessment of the contribution of human-driven global warming to MHW is necessary to understand how MHW and their underlying drivers respond to global warming and how these responses

Author affiliations: [a]Mediterranean Institute for Advanced Studies (CSIC-UIB), Spain ; [b]Department of Physics, University of the Balearic Islands, Spain; [c]International Space Science Institute, Switzerland; [d]National Centre for Atmospheric Science and Department of Meteorology, University of Reading, United Kingdom

MM and AA conceived and designed the study. MM produced the counterfactual method and outputs. MM, AA and MA analysed the data. All authors contributed to the discussion of the results. MM wrote the manuscript with contributions from all authors.

Authors declare no competing interests.

[2]To whom correspondence should be addressed. E-mail: marta.marcos@uib.es

*From Copernicus Climate Change Service and Copernicus Marine Service: https://climate.copernicus.eu/record-breaking-north-atlantic-ocean-temperatures-contribute-extreme-marine-heatwaves and https://marine.copernicus.eu/news/2023-northern-hemisphere-summer-record-breaking-oceanic-events

are distributed geographically. Quantifying the impact of changing surface air temperature on SST and on MHW serves to anticipate how they will evolve in the forthcoming years as global warming intensifies (2, 17), and which will be the implications for vulnerable marine ecosystems and their adaptive capabilities, and the loss of associated ecosystem services for human societies (6). Here, we address this question by calculating the contribution of long-term increasing surface air temperature to observed global SST fields since 1940. We use this relationship to construct a counterfactual SST climate, that corresponds to the observed SST without the effect of increasing global temperature, while keeping local and regional variability unchanged. Unlike earlier works based on probabilistic event attribution from an ensemble of climate models (9, 15), our study quantifies the relationship between the observed SST evolution and long-term changes in globally averaged surface air temperatures to provide a quantitative assessment of the changes in SST attributed to global rising temperatures, instead of a probabilistic one. Also, differently from other approaches based solely on observations, the impact of long-term global temperature rise on SST and, therefore on MHW, is quantified by comparing observed and counterfactual SST, without defining baseline periods. Therefore, our approach provides a tool for attribution that permits calculating the influence of global increasing temperatures in MHW by simply subtracting its counterfactual version to the observed event.

## SST changes linked to long-term surface air temperature trends

We quantify the contribution of increasing global surface air temperature to the intensity and persistence of MHW over the world oceans by comparing SST observations with a counterfactual version of SST in which there has been no global temperature change for the period 1940-2023 (see Materials and Methods). Specifically, the counterfactual SST represents a hypothetical SST for which the long-term signals correlated with global surface air temperature changes have been removed locally, while the observed short-term variability remains unchanged. Note that, by accounting only for the low-frequency changes in surface warming, we keep natural variability for periods shorter than ∼10 years in the global average unaltered in the counterfactual SST, including major signals linked to large-scale patterns such as ENSO. Other internal variability in the globally averaged surface temperature with periods longer than 10 years is removed in the counterfactual fields. However, the contribution of this long-term filtered natural variability to global increase in surface temperature is much smaller than the long-term changes linked to anthropogenic component, especially after 1960 (18, 19). Indeed, on the basis of climate attribution studies (20, 21), it has been established that the observed long-term increase in global surface air temperature since the mid-$20^{th}$ century is of anthropogenic origin (18, 19). We also show that the impact of natural variability in filtered globally averaged surface air temperature is negligible when computing the counterfactual SST fields (see Materials and Methods). Therefore, by removing this contribution from observations, the counterfactual SST corresponds to a version of SST without the effect of human-induced global warming, at least since 1960, and that contains only internal climate variability, while preserving the observed chronology (see Materials and Methods section for details). The counterfactual temperatures thus provide a baseline to determine the attribution of anthropogenic global warming on the observed local temperature variability and MHW.

We illustrate the impact of increasing global surface air temperatures in SST patterns during three extreme events that have been identified as prominent MHW. Figure 1 displays observed and counterfactual SST for the Northeast Pacific MHW event of 2014-15 (10), for the MHW event in the Tasman Sea in 2015-16 (11) and the recent MHW in the Mediterranean Sea in 2023. The contribution of global warming to the intensity of these three events, quantified as the differences between observed and counterfactual SST (black lines), indicates values below $1^{\circ}C$, with a maximum of $0.8^{\circ}C$ [0.3 - $1^{\circ}C$] (uncertainties provided hereinafter correspond to the standard deviation) for the Northeast Pacific MHW, up to $1.5^{\circ}C$ [1.3 - $1.8^{\circ}C$] for the Tasman Sea event and in excess of $2^{\circ}C$ [1.4 - $2.5^{\circ}C$] over the Mediterranean Sea during the summer seasons in 2022 and 2023. In the Northeast Pacific region (upper panels), in 2014-15, observed SST time series is well above the long-term climatology (defined here as the mean SST values during 1980-2015, following (10)), but so does the counterfactual SST record, indicating that the occurrence and intensity of this event is partly driven by natural climate variability. In particular, during winter 2015 the MHW intensity is $\sim 2^{\circ}C$ above the climatology, of which only $\sim 0.75^{\circ}C$ [0.5 - $1^{\circ}C$] are linked to global surface air temperature warming. Conversely, for the Tasman Sea event (middle panels), during year 2016, counterfactual SST is close to the climatological values (here defined as the mean SST during 1982-2005, following (11)). The MHW in the Tasman Sea during the Austral summer 2015-16 has been reported as the most intense in the region (11), and these results show that it is almost entirely attributed to global warming. This agrees with the findings in (11) who concluded that it is virtually certain that anthropogenic climate change has increased the likelihood of the intensity and duration of this event. Finally, the temporal evolution of observed and counterfactual SST over the central Mediterranean Sea during the period 2021-23 (lower panels), reveals the exceptionally warm summers within this period, with positive contributions of global warming exceeding $2^{\circ}C$ systematically every year. Note that although the largest SST values in this region were observed in summer 2023, the contribution of global warming was even larger in summer 2022. These three examples showcase the use of the counterfactual SST as a tool to quantify the impact of human-induced global warming on the intensity and likelihood of MHW events.

## Quantification of the impact of global warming in MHW

We calculate MHW with observed and counterfactual daily SST similar to (1) (see Methods). We first explore the changes in the persistence of MHW since 1940 and their link to globally increasing surface air temperatures. We define the persistence of MHW for each year as the cumulative number of days that every grid point experiences a MHW in observed and counterfactual climates. We find that, globally, the average number of days under MHW conditions evolves from 15.3 days/year (constant during the period 1940-1960) to 48.8

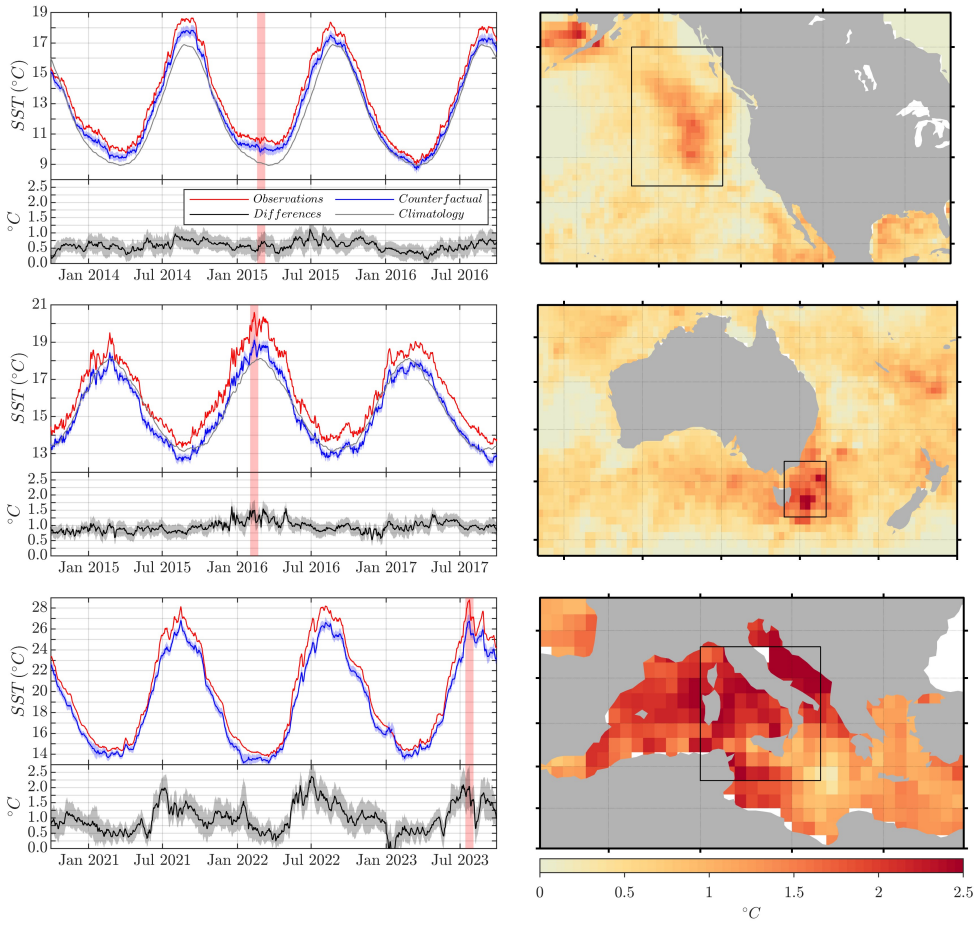


**Fig. 1. Observed and counterfactual SST during three MHW episodes.** Left column shows the temporal evolution of observed SST (red lines), of its counterfactual SST (blue lines) and their differences (black lines) with uncertainties (shadow areas) for three MHW events in the Northeast Pacific (10), the Tasman Sea (11) and the Mediterranean Sea, averaged over the boxes in the maps of the right column. Also shown are the SST climatologies in the top and middle panels, defined as in (10) and (11), respectively, where these two events were first described and analysed. Right column maps the differences between observed and counterfactual SST for the time indicated by vertical grey shading in the panels of the left column.

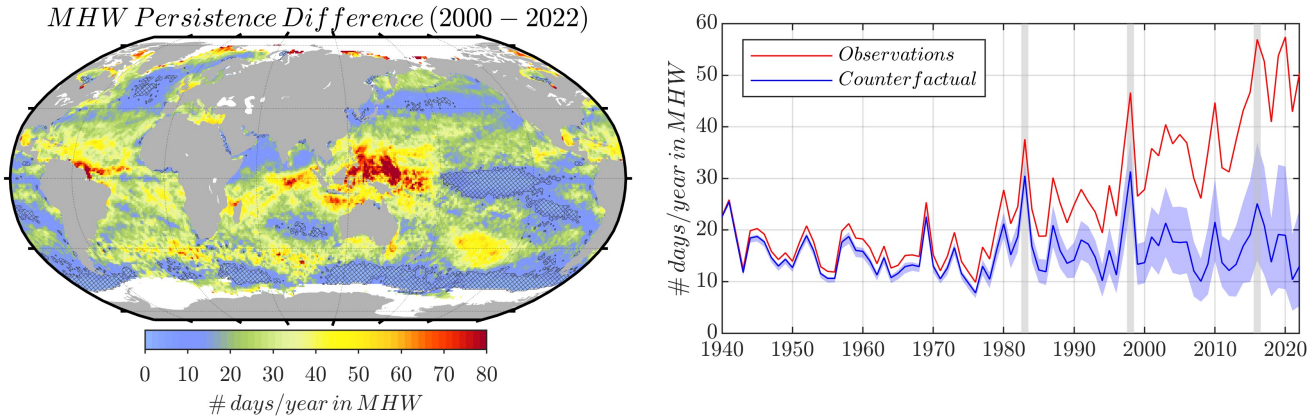


**Fig. 2. Impact of global warming on the persistence of MHW conditions.** The map shows point-wise differences of the number of days per year experiencing a MHW between observed and counterfactual SST, averaged over 2000-2022. Hatched areas correspond to regions where the change is smaller than the uncertainty. Right panel shows yearly globally-averaged number of days under MHW conditions in counterfactual (blue) with uncertainties corresponding to the standard deviation (shadow area) and observed (red) SST during 1940-2022. Vertical shadowed bands indicate very strong El Niño events.

days/year in the last 5 years (2018-2022) in observed SST (red line in Fig. 2).

By contrast, in the counterfactual SST (blue line in Fig. 2), this metric remains nearly unchanged, with an average of 15.8 days/year from 1940 to 2022. In comparison, observations show a globally averaged increase of 34 days/year [23-42 days/year] for the period 2018-2022, representing a three-fold rise in MHW days linked to global warming since 1940. This indicates an increase in the likelihood of experiencing MHW events from 4% up to 13% on average. Regionally, the greatest increases occur in the equatorial/tropical western Pacific and Indian oceans and equatorial Atlantic, where MHW days rise by up to 80 days/year (20% of increased likelihood) over 2000-2022 (Fig. 2).

Despite this, the observed and counterfactual climates show consistent interannual variability in the number of MHW days (Fig. 2), with strong El Niño years (shadowed bands in Fig. 2) standing outprominently in both time series, reflecting that it is a major global driver of MHW on interannual timescales (7, 22). This is expected since in the counterfactual SST removes only changes correlated with long-term trends in global surface air temperature, preserving natural variability induced by climate patterns, such as El Niño.

Global warming contributes to increased MHW intensity as well. Comparing observations with counterfactual SST anomalies reveals a mean rise of $1°C$ [0.7 - $1.3°C$] globally since 1940, with most of this increase ($0.85°C$) occurring since 1981 (right panel of Fig. 3), coinciding with the rapid increase in global surface air temperature (Fig. S2). Spatial patterns averaged over 2000-2022 show amplified intensities in western boundary currents, the central South Pacific, the Mediterranean Sea, the Arctic Ocean, and shallow areas like the North and Baltic Seas, where SST increases surpass $1.5°C$. These regions partially overlap with those hosting the most intense MHWs, though in others, such as the Mediterranean and central South Pacific, temperature anomalies during MHW events remain below $0.5°C$ (8). Overall, MHW intensity has increased mostly outside of the Tropics, with equatorial regions and the Southern Ocean displaying below average or negligible impact of global surface air temperatures on MHW intensity (Fig. 3). This is because, in higher latitudes, the ocean's capability to absorb heat is enhanced by greater temperature contrasts and less intense heat loss than in the Tropics.

Since 1940, the ocean surface has warmed by $0.5°C$, mostly since mid-1970s (see Fig. S2), whereas the impact of anthropogenic warming on MHW events is twice this value globally (Fig. 3). Consequently, changes in MHW driven by global warming are only partly associated with shifting mean SST. The comparison of changes in the intensity of MHW and in the mean SST (Fig. 3 and S2, respectively) reveals that in regions as the central South Pacific, the Japan Sea and Southeast Australia, the increased rate of MHW intensity is similar to that of the SST trend, thus indicating that global warming impacts the intensity of MHW primarily by rising mean SST. Conversely, in the Mediterranean and North Seas, the increase in the intensity of MHW episodes doubles the amplitudes of the mean SST increase. This means that other factors, such as changes in the variability of SST (for example, a greater number of warm days) are also a driving mechanism of MHW in some regions. These results are in agreement with (15), who found that externally-forced changes in mean SST were affecting globally the intensity of MHW, while some regions were also impacted by changes in the variance. In the Tropical regions, for example, where averaged SST is the highest and the ocean absorbs less net heat, MHW are extended in duration rather than in intensity. Thus, the largest changes in the persistence of MHW conditions, that occur predominantly in the equatorial west Atlantic and west Pacific oceans, are not driven by the fast changes in mean SST, indicating that the SST variability is playing a dominant role in these regions. This combination of changes in mean and variance of the SST impacting on MHW intensity was also found and discussed by (15).

## Conclusions

We found that the contribution of the increasing global surface temperature to MHW, quantified via the comparison between observed SST data against its counterfactual version,

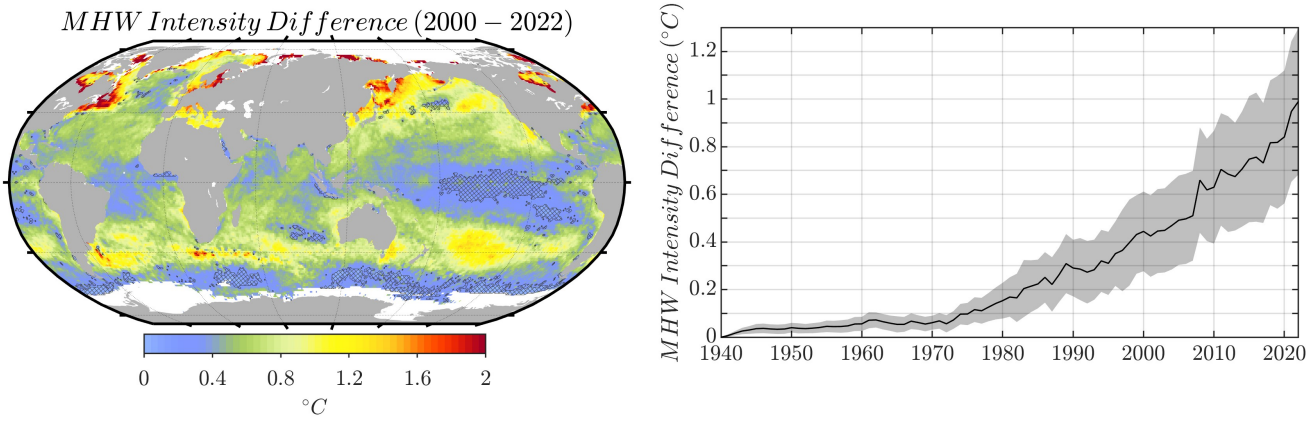


**Fig. 3. Increase in MHW intensity driven by global warming.** The map displays the differences in SST anomalies between observations and counterfactual climate during observed MHWs, averaged over 2000-2022. Hatched areas correspond to regions where the change is smaller than the uncertainty. Right panel shows yearly globally-averaged differences for the period 1940-2022 with uncertainties corresponding to the standard deviation.

is a steady and continuous globally averaged rise in the maximum intensity of the observed MHW reaching $1 \pm 0.3°C$ in 2020s and a three-fold increase in the number of days that the oceans are under extreme MHW conditions in the recent years with respect to 1940. Thus, observed global warming, most of which is human-induced, is currently the dominant contributor to the upward trends in these MHW metrics. These results are in line with (9) who computed the fraction of attributable risk for MHW and identified a strong anthropogenic impact on major MHW occurred in the last 15 years. Our approach goes a step beyond and permits quantifying that, without global warming, the 47% of the observed number of MHW during the period 2000-2020 would have not been identified as extreme events.

Observed changes in MHW characteristics are geographically heterogeneous (8, 12), meaning that the impact of global warming varies with regions. Specifically, global warming is responsible of at least 70% of the observed intensity in MHW in half of the oceans' surface, and it also drives at least 50% of the observed number of days under MHW conditions over 65% of the ocean areas. The spatial patterns of the changes in MHW characteristics also show that there are regions where global warming enhances both intensity and persistence of MHW conditions and regions where either one or the other are responding to increased global surface air temperature. In the equatorial and tropical eastern Pacific and eastern Atlantic Oceans and in the equatorial Indian Ocean, MHW conditions become more frequent but not more intense due to global warming. Conversely, in western boundary currents in the North Atlantic and North Pacific and in the Baltic Sea, the opposite is true, as MHW gain intensity but do not increase their persistence due to global warming. In the central South Pacific, southwestern Australia, the Arctic and the North Sea, both intensity and frequency increase in response to global warming. These different changes in MHW properties can have profound impacts on the adaptation of marine ecosystems to new climatic conditions, that respond to a combination of extreme heat and event duration (4, 23).

The methodology developed here is transferable to other climate variables and can be used to perform attribution studies by providing quantitative information on the role of global warming on the observed changes at local and regional scales. Given that human-induced global warming will likely continue in the future, unravelling the relationship between this forcing and the local changes in climate variables serves to anticipate future changes and climate-related hazards and damages, and supports the definition of realistic climate and biodiversity targets and the design of mitigation and adaptation strategies.

**Data Archival.** SST anomalies and dates of MHW in ERA5 and the simultaneous SST anomalies in counterfactual SST are available at https://doi.org/10.5281/zenodo.10522831

**Supporting Information Appendix (SI).** See File.

**SST data.** Daily SST fields for the global ocean were obtained from the fifth-generation atmospheric reanalysis produced by the European Centre for Medium-Range Weather Forecasts (ERA5) (24) (last access October 15, 2023). These fields have been produced combining different observational products (25). Specifically, SST fields in ERA5 are generated using monthly HadISST version 2 data (26) until 1960, pentadal HadISST version 2 data between 1961 and August 2007 and OSTIA daily satellite product (27) afterwards (28). It has been shown that HadISST and OSTIA products show consistent large-scale variability, which justifies their combination into a single record (25). Nevertheless, changing observing systems over time may introduce inhomogeneities, especially at small-scales. Data are provided over a 0.25°x0.25° mesh starting in January 1940, and they were averaged out spatially onto a 1°x1° grid.

**Construction of counterfactual SST fields.** Counterfactual SST fields are versions of SST climate for which the long-term climate trends, represented by the globally-averaged 2-m air temperature, have been removed locally. The methodology applied here to construct counterfactual SST fields is similar to (29), who computed stationary counterfactual climates for observational fields of various atmospheric variables over land, using global surface air temperatures as a predictor for detrending observations. We follow (29) and use globally-averaged 2-m air temperature ($SAT_{global}$) as the proxy for

long-term climatic trend. $SAT_{global}$ was calculated from monthly gridded air temperatures obtained from ERA5 reanalysis with a spatial resolution of 0.25°x0.25° for the period 1940 onward (24). After being globally averaged, $SAT_{global}$ was low-pass filtered using Singular Spectrum Analysis with an embedding dimension of 10 years, to retain only long-term changes. The resulting curve is shown in Figure S2 (inset panel).

The procedure to construct the counterfactual SST fields is represented schematically in Figure S1. Each time series of SST at every grid point was analysed separately. First, from the complete daily record (Fig. S1a), we define 365 calendar-day time series, from January 1st to December 31st (note that we remove all February 29 days), for the period 1940-2022. Each of these calendar-day time series contains thus 83 values, one for each year. Figure S1b displays two examples of yearly SST time series for January 1st and September 1st. These yearly SST records were modelled as normal distributions for which the mean and the variance are allowed to change over time. Figure S1c shows the empirical distributions of the two example time series for two periods of time, namely before and after 1980. It is shown that the probability distributions are different and shifted towards warmer values in the most recent period. This temporal variability in the parameters of the normal distribution was defined dependent on $SAT_{global}$ as follows:

$$\begin{aligned} SST(i,j,t_{day}) &\sim \mathcal{N}(\mu,\, \sigma^2) \\ \mu = \mu(SAT_{global}) &= a_1 SAT_{global} + a_2 \\ \sigma = \sigma(SAT_{global}) &= \exp(b_1 SAT_{global} + b_2) \end{aligned} \qquad [1]$$

where $a_1$, $a_2$, $b_1$ and $b_2$ are constants calculated at every grid point and for each calendar-day record. Therefore, 365x4 parameters (2 for $\mu$ and 2 for $\sigma$) were adjusted for every daily SST time series. We have tested the assumption of normal distribution of calendar-day records using a Kolmogorov-Smirnov test. We found that over most of the ocean, calendar-day SST distributions can be considered Gaussian throughout the entire year. This condition is not fulfilled in high latitudes, very likely due to the presence of sea ice during the winter. Therefore, we remove all the values that are not normally distributed in the calculations of the counterfactual SST fields (they represent 12% of the total values and are concentrated in high latitudes). Our approach differs from (29) in that we do not prescribe either the shape or the changes in seasonality, as we analyse independently every calendar day. This means that if summer or winter SST are responding differently to changes in $SAT_{global}$ this is reflected in the variability of the coefficients of the normal distributions that are computed separately. This approach, therefore, naturally accommodates changes in seasonality. Unlike in (29) we also allow for changes in the variance of the distribution in response to increased global temperatures (note the exponential definition because this parameter must be defined positive). We used a Bayesian framework to fit the distributions with weakly informative priors for all four parameters. More specifically, we set zero-centred and unit variance normal distributions for $a_{1,2}$ and $b_{1,2}$. The statistical model has been implemented in *Stan* (30), a state-of-the-art probabilistic programming language that provides Bayesian statistical inference with Markov Chain Monte Carlo (MCMC) sampling. The model has been run through the *R* interface with the toolbox *cmdstanr* (31) using four parallel chains of 1,000 iterations each (of which 500 correspond to warming-up).

Once the parameters of the distributions were determined for the SST time series, the counterfactual distributions were constructed setting $SAT_{global}$ constant at a given initial time. The values of the means $\mu$ and variances $\sigma$ of the normal distributions of the counterfactual climate have thus constant values, given by the parameters $a_2$ and $b_2$. We recall here that $SAT_{global}$ has been low-pass filtered, which implies that only long-term changes in globally-averaged surface warming are removed when this variable is set constant, whereas variations in global surface air temperature with periods shorter than ∼10 years are retained in the counterfactual fields. SST variability linked to regional variations in surface air temperature were also retained, as only those correlated with global changes in air temperature were removed. The counterfactual time series were then calculated through quantile mapping (Figure S1e). To do so, we calculate the quantile of a given SST value in the observed time series using the corresponding normal distribution (i.e., estimated with temporally varying mean and variance). In the examples of Figure S1, the CDFs of these distributions are represented in panel *e* as thick lines. Then, we seek the SST value that corresponds to the same quantile in the counterfactual distribution (with constant mean and variance, and represented as thin lines in Figure S1e). We repeat the process for every daily value in the SST records at each grid point, resulting in the daily counterfactual SST (Figure S1f). This approach preserves the real chronology and local variability of SST, and allows the quantification of the contribution of the observed long-term trend in globally-averaged air temperature to observed SST at every grid point. Therefore, the resulting counterfactual SST time series represent the observed local and regional variability, but in a climate in which long-term changes in global air temperatures have stopped since a defined time origin. Note that this time origin is arbitrary and does not alter the relationship between SST and global air surface temperature (i.e., does not affect the evolution of counterfactual SST). Since in the counterfactual SST only changes correlated with long-term trends in global surface air temperature have been removed, it is expected to keep natural variability induced by climate patterns, such as El Niño, unaltered.

Despite being globally-averaged and low-pass filtered, there is still some natural variability remaining in $SAT_{global}$. We have quantified this variability using the climate simulations of the experiment *Historical-Nat* available for 12 models in CMIP6 data repository. This experiment contains only natural changes in radiative forcing and excludes anthropogenic sources. Gridded surface air temperatures for every climate model have been globally averaged and filtered in the same way as $SAT_{global}$(Fig. S2). The mean curve, representative of natural variability, has been removed from $SAT_{global}$. The new proxy has been used to calculate the counterfactual SST time series for a selected set of grid points, spaced 20° degrees in latitude and longitude and located between ±50° in latitude, resulting in a total of 70 points globally distributed. The differences between counterfactual time series computed with and without natural variability in the proxy are negligible in the subset of grid points, thus indicating that there is no impact of this low-pass filtered,

globally averaged natural variability on counterfactual SST fields.

Other detrending methods, such as linear regression of the observed record over a predictor, may result in large regional errors, especially when the predictor also contains significant internal variability (32, 33). This is not the case here, as low-pass filtered $SAT_{global}$ (Fig. S3, inset panel) essentially reflects the impact of long-term global warming, especially since 1960 (18). Also, in regions with large variance in SST, the signal-to-noise ratio between the forced component and natural high-frequency variability is low, which may underestimate the contribution of the predictor. Thus, unlike other more simple methods, our approach is able to capture the impact of the changes of $SAT_{global}$ on local SST even in regions with large SST variance. In absence of observations of a hypothetical counterfactual climate, a validation of the methodology is provided using climate model simulations through the comparison of counterfactual SST with a pre-industrial control run (see section on Validation below). We have produced a counterfactual climate for ERA5 global SST, for the period 1940 onwards, at 1°x1° spatial resolution and setting the global temperature at its value in 1940.

The Bayesian framework provides a probability density function of each of the four parameters ($a_1$, $a_2$, $b_1$ and $b_2$) in equation 1, which we modelled to be normally distributed in our prior assumptions. We use their standard deviations to estimate the uncertainties associated to the counterfactual SST fields. To do so, we sample the distributions of the parameters 200 times and construct the same number of counterfactual time series are each grid point, as described above. The uncertainty of the counterfactual SST time series for a given grid point is then calculated as the standard deviation of the 200 time series. Therefore, every counterfactual SST time series is accompanied by its temporally-varying uncertainty bounds.

Globally averaged time series of SST from ERA5 and from its counterfactual version are plotted in Fig. S3. SST has increased at a mean global rate of $0.066 \pm 0.005°C/decade$ since 1940 ($0.13 \pm 0.01°C/decade$ since 1981), a value that has been rising up to $0.14 \pm 0.02°C/decade$ in the most recent period 2000-2022. The acceleration computed wit ha quadratic fit is $0.018 \pm 0.003°C/decade^2$ since 1940 ($0.018 \pm 0.006°C/decade^2$ since 1960). These values contrast with those derived from the counterfactual SST time series, that display a globally-averaged linear trend of $0.010 \pm 0.004°C/decade$ since 1940 (and $0.034 \pm 0.009°C/decade$ since 1981) and $0.02 \pm 0.02°C/decade$ in 2000-2022. For counterfactual SST, the global acceleration is $0.006 \pm 0.003°C/decade^2$ since 1940 ($0.01 \pm 0.01°C/decade^2$ since 1960). The different rates between ERA5 and its counterfactual version results in global warming being responsible of SST warming by $0.50 \pm 0.27°C$ since 1940 (accounting for method uncertainties), of which half ($0.24 \pm 0.20°C$) has occurred since year 2000.

**Definition of marine heatwaves (MHW).** We used the definition of (1) to calculate MHW from SST fields. Here, MHW events were calculated at every grid point as periods of 7 days or longer during which SST exceeded the $95^{th}$ percentile of the averaged local SST between 1940 and 1970 of ERA5. The 30-year reference period has been chosen as the longest period when $SAT_{global}$ remains nearly unchanged (see inset in top panel in Fig. S3). The same threshold has been used for the real and the counterfactual time series. Since the changes of $SAT_{global}$ in this period are small compared to the most recent decades, both realisations are consistent to each other, with a median difference in the thresholds of only $0.04°C$. We define a constant threshold instead of a time shifting baseline period to reflect the temporal evolution of extreme conditions (34). We do not vary our threshold seasonally because we focus on summer MHW events. Setting a different percentile for the threshold would change the number of events but neither their temporal evolution nor their spatial features.

For every MHW event, we calculated the maximum SST anomalies, its duration and timing. In addition, the counterfactual SST anomalies corresponding to the ERA5 MHW events were also extracted to calculate the contribution of long-term $SAT_{global}$ changes to observed MHW. MHW with a difference in SST anomalies between real and counterfactual climates exceeding $6°C$ we removed; this was the case in 950 grid points (about 2% of the total number of grid points) all located at high latitudes in the northern hemisphere, thus suggesting that the presence of sea ice affects negatively to the computation of the counterfactual SST. The averaged results of the characteristic MHW in ERA5 are mapped in Fig. S4.

**Validation of the counterfactual approach.** The methodology developed to compute the counterfactual climate has been validated using the SST fields from the climate model $GFDL\_ESM4$ (35). Daily gridded SST fields with 1°x1° resolution from the pre-industrial control runs, spanning 500 years, and one of the historical runs for the period 1850-2014 have been downloaded from $ESGF@DOE/LLNL$ node (https://esgf-node.llnl.gov/search/cmip6/). Monthly gridded 2-m air temperature fields were also obtained for the historical run for the period 1850-2014. Globally-averaged air surface temperature has been computed from gridded data and the resulting time series has been low-pass filtered in the same manner as that of ERA5 explained above, and has been used as the predictor for the long-term climate signal of the historical run. The counterfactual SST of the historical run was constructed as described above and compared to the pre-industrial control run in terms of the temporal variability of SST and the evolution of changes in MHW. Since the historical and pre-industrial model simulations correspond to two different climate realisations with different chronologies, we perform the comparisons in terms of statistical values. Note that the temporal evolution of low-frequency global surface air temperature over the $20^{th}$ century (inset in Fig. S6) is not steady over time, as a result of the combination of greenhouse gases and aerosol forcings (19). This variability, irrespective of its origin, will be captured in the dependence between SST and $SAT_{global}$. This means that the counterfactual SST computed from the historical simulation will not contain the effect of these changes in $SAT_{global}$ and will, therefore, be comparable to the pre-industrial control simulation that only accounts for natural variability.

Linear trends of historical SST are mapped in Fig. S5 for the period 1940-2014. SST trends are positive in 85% of the ocean surface with an average value of 0.05 °C/decade. Negative trends are found in the subpolar North Atlantic and North Pacific oceans. In contrast, counterfactual SST trends are on average 0.005 °C/decade for the same period with a

much smoother spatial pattern. Four grid points from different regions showing distinct behaviours have been selected and their 10-year-window SST histograms are represented in Fig. S5 centred at three different years corresponding to initial (year 1875), intermediate (1965) and late (2008) periods of simulation. The natural variability of SST at each of these grid points is represented as the grey shadowed areas corresponding to the region covered by the 490 10-year-window SST histograms of the 500 years of pre-industrial control run. Historical (red lines) and counterfactual (blue lines) SST histograms are indistinguishable in the first two times and diverge in the recent period. Notably, it is shown that the counterfactual SST records lie within the natural variability of SST at all times, whereas SST from the historical simulation is outside natural variability during the most recent period.

The temporal evolution of globally-averaged SST is plotted in Fig. S6 for the historical and counterfactual climates, together with the global averaged low-pass filtered 2-m air temperature (inset in the figure). Differences between yearly variations in historical (red line) and counterfactual (blue line) globally-averaged SST follow the long-term trend in changes in global surface air temperature. Note that all low-frequency changes in surface warming are captured by the method, including slightly decreasing trends in 1940-1960, that in the observations have been linked to the combination of greenhouse gases and aerosols (19), and that are reproduced by the historical temperatures of the climate model. When compared to natural variability computed from the pre-industrial control run (grey shadowed area), yearly variations of the counterfactual SST are within its range during the entire period 1850-2014. Conversely, historical SST (red line) separates from natural variability in periods of changing global temperatures. In particular, since approximately 1990, historical SST shows a clearly distinct behaviour from the counterfactual values. The differences between historical and counterfactual climates have also been evaluated for MHW, here computed with a baseline period 1850-1900. The fraction of the ocean surface that record a MHW in the historical simulation (Fig. S7) varies over time consistently with changes in mean global surface air temperature. While MHW in the counterfactual climate (blue lines) lie within natural variability, MHW in the historical climate increase drastically since 1990 globally.

In summary, the SST variability of the counterfactual version of the historical climate simulation is consistent with that of the pre-industrial climate. These results indicate that the impact of long-term trends linked to increasing global temperature in the historical run have been successfully removed in the counterfactual SST, thus providing a robust validation of the methodology.

**ACKNOWLEDGMENTS.** This research was funded by DRICOEX project, grant number CNS2022-135532, funded by MCIN/AEI/10.13039/501100011033 and by "European Union NextGenerationEU/PRTR". It was also partially funded by DETECT project (reference PID2021-124085OB-I00 MCIN/AEI/10.13039/501100011033/FEDER,UE). JR was funded by NERC via the CANARI (NE/W004984/1) and WISHBONE (NE/T013516/1) projects. The authors are grateful to Prof. Robert van Woesik and Prof. Ed Hawkins for providing comments on the manuscript.

1. AJ Hobday, et al., A hierarchical approach to defining marine heatwaves. *Prog. Oceanogr.* **141**, 227–238 (2016).
2. TL Frölicher, C Laufkötter, Emerging risks from marine heat waves. *Nat. Commun.* **9** (2018).
3. TP Hughes, et al., Global warming and recurrent mass bleaching of corals. *Nature* **543**, 373–377 (2017).
4. N Marbà, CM Duarte, Mediterranean warming triggers seagrass (posidonia oceanica) shoot mortality. *Glob. Chang. Biol.* **16**, 2366–2375 (2010).
5. T Wernberg, et al., Climate-driven regime shift of a temperate marine ecosystem. *Science* **353**, 169–172 (2016).
6. DA Smale, et al., Marine heatwaves threaten global biodiversity and the provision of ecosystem services. *Nat. Clim. Chang.* **9**, 306–312 (2019).
7. M Collins, et al., *Extremes, Abrupt Changes and Managing Risk*, eds. HO Portner, et al. (Cambridge University Press, Cambridge, United Kingdom and New York, NY, USA), pp. 589–655 (2019).
8. ECJ Oliver, et al., Longer and more frequent marine heatwaves over the past century. *Nat. Commun.* **9** (2018).
9. C Laufkötter, J Zscheischler, TL Frölicher, High-impact marine heatwaves attributable to human-induced global warming. *Science* **369**, 1621–1625 (2020).
10. E Di Lorenzo, N Mantua, Multi-year persistence of the 2014/15 north pacific marine heatwave. *Nat. Clim. Chang.* **6**, 1042–1047 (2016).
11. EC Oliver, et al., The unprecedented 2015/16 tasman sea marine heatwave. *Nat. Commun.* **8** (2017).
12. NJ Holbrook, et al., A global assessment of marine heatwaves and their drivers. *Nat. Commun.* **10** (2019).
13. B Fox-Kemper, et al., *Ocean, Cryosphere and Sea Level Change*, eds. V Masson-Delmotte, et al. (Cambridge University Press, Cambridge, United Kingdom and New York, NY, USA), p. 1211–1362 (2021).
14. Y Yao, J Wang, J Yin, X Zou, Marine heatwaves in china's marginal seas and adjacent offshore waters: Past, present, and future. *J. Geophys. Res. Ocean.* **125**, e2019JC015801 (2020) e2019JC015801 2019JC015801.
15. L Dong, et al., Roles of external forcing and internal variability in global marine heatwaves change during 1982–2021. *Geophys. Res. Lett.* **51**, e2023GL107557 (2024) e2023GL107557 2023GL107557.
16. E Weller, et al., Human contribution to the 2014 record high sea surface temperatures over the western tropical and northeast pacific ocean. *Bull. Am. Meteorol. Soc.* **96**, S100 – S104 (2015).
17. Y Cheng, et al., A quantitative analysis of marine heatwaves in response to rising sea surface temperature. *Sci. The Total. Environ.* **881**, 163396 (2023).
18. V Eyring, et al., *Human Influence on the Climate System*, eds. V Masson-Delmotte, et al. (Cambridge University Press, Cambridge, United Kingdom and New York, NY, USA), p. 423–551 (2021).

19. GA Meehl, et al., Combinations of natural and anthropogenic forcings in twentieth-century climate. *J. Clim.* **17**, 3721 – 3727 (2004).
20. A Ribes, FW Zwiers, JM Azaïs, P Naveau, A new statistical approach to climate change detection and attribution. *Clim. Dyn.* **48**, 367–386 (2017).
21. A Hannart, P Naveau, Probabilities of causation of climate changes. *J. Clim.* **31**, 5507 – 5524 (2018).
22. A Sen Gupta, et al., Drivers and impacts of the most extreme marine heatwaves events. *Sci. Rep.* **10** (2020).
23. S Sully, DE Burkepile, MK Donovan, G Hodgson, R van Woesik, A global analysis of coral bleaching over the past two decades. *Nat. Commun.* **10** (2019).
24. H Hersbach, et al., Era5 monthly averaged data on single levels from 1940 to present. (2023) Copernicus Climate Change Service (C3S) Climate Data Store (CDS).
25. S Hirahara, M Alonso-Balmaseda, E de Boisseson, H Hersbach, *Sea Surface Temperature and Sea Ice Concentration for ERA5* (ECMWF), (2016).
26. HA Titchner, NA Rayner, The met office hadley centre sea ice and sea surface temperature data set, version 2: 1. sea ice concentrations. *J. Geophys. Res. Atmos.* **119**, 2864–2889 (2014).
27. S Good, et al., The current configuration of the ostia system for operational production of foundation sea surface temperature and ice concentration analyses. *Remote. Sens.* **12** (2020).
28. H Hersbach, et al., The era5 global reanalysis. *Q. J. Royal Meteorol. Soc.* **146**, 1999–2049 (2020).
29. M Mengel, S Treu, S Lange, K Frieler, Attrici v1.1 – counterfactual climate for impact attribution. *Geosci. Model. Dev.* **14**, 5269–5284 (2021).
30. Stan Development Team, Stan modeling language users guide and reference manual (2023).
31. J Gabry, R Češnovar, *cmdstanr: R Interface to 'CmdStan'*, (2022) https://mc-stan.org/cmdstanr/, https://discourse.mc-stan.org.
32. C Deser, AS Phillips, Spurious indo-pacific connections to internal atlantic multidecadal variability introduced by the global temperature residual method. *Geophys. Res. Lett.* **50**, e2022GL100574 (2023) e2022GL100574 2022GL100574.
33. C Frankignoul, G Gastineau, YO Kwon, Estimation of the sst response to anthropogenic and external forcing and its impact on the atlantic multidecadal oscillation and the pacific decadal oscillation. *J. Clim.* **30**, 9871 – 9895 (2017).
34. A Sen Gupta, Marine heatwaves: definition duel heats up. *Nature* **617** (2023).
35. JP Dunne, et al., The gfdl earth system model version 4.1 (gfdl-esm 4.1): Overall coupled model description and simulation characteristics. *J. Adv. Model. Earth Syst.* **12**, e2019MS002015 (2020).